

Twist, splay, and uniform domains in ferroelectric nematic liquid crystals

Maxim O. Lavrentovich*

*Department of Earth, Environment, and Physics,
Worcester State University, Worcester, Massachusetts 01602, USA and
Department of Physics & Astronomy, University of Tennessee, Knoxville, Tennessee 37996, USA*

Priyanka Kumari

*Advanced Materials and Liquid Crystal Institute,
Kent State University, Kent, Ohio 44240, USA and
Materials Science Graduate Program, Kent State University, Kent, Ohio 44240, USA*

Oleg D. Lavrentovich†

*Advanced Materials and Liquid Crystal Institute, Kent State University, Kent, Ohio 44240, USA
Materials Science Graduate Program, Kent State University, Kent, Ohio 44240, USA and
Department of Physics, Kent State University, Kent, Ohio 44240, USA*

The recently-discovered ferroelectric nematic (N_F) liquid crystal presents a host of defect phenomena due to its unique polar nature and long-ranged electrostatic interactions. Like the solid state ferroelectrics, the depolarization field in the material favors a spontaneous spatial variation of the polarization \mathbf{P} , manifesting in myriad ways including a twist in the bulk and different arrangements of alternating polarization domains. Unlike the solid-state ferroelectrics with a bulk crystalline structure, the configuration of the N_F fluids is determined not only by the reduction of depolarization fields but also by the alignment of molecules at interfaces. In this work, we consider an N_F confined to a thin cell, pre-patterned with various types of apolar surface anchoring produced by photoalignment. For uniform planar alignment, we find that the sample forms a series of striped domains. For a cell pre-patterned with a radial +1 defect pattern, the N_F breaks up into “pie-slice” polarization domains. We calculate the elastic and electrostatic energy balance which determines the observed configurations and demonstrate that the electrostatic interactions tend to decrease the characteristic domain size λ while the elastic and surface anchoring interactions facilitate a larger λ . We also demonstrate that ionic screening mitigates electrostatic interactions, increasing λ and, above some critical concentration, eliminating the domains altogether.

I. INTRODUCTION AND BACKGROUND

The polar ordering of the recently discovered ferroelectric nematic (N_F) liquid crystal [1–4] creates a fascinating interplay between the elasticity, surface interactions, and the electrostatic energy associated with spatial variations of the spontaneous polarization \mathbf{P} . The ensuing N_F structures are not restricted by crystallographic axes and can be studied by polarizing optical microscopy since, in the materials explored so far, the polarization \mathbf{P} is along the optic axis, or the director $\hat{\mathbf{n}}$.

N_F structures tend to avoid a splay deformation (divergence of \mathbf{P}) since it creates a bound charge of a bulk density $\rho = -\nabla \cdot \mathbf{P}$ and increases the electrostatic energy. Polarization-related charges are also avoided at surfaces and at domain walls. For example, a uniform polarization, $\mathbf{P}(x, y, z) = \text{const.}$, would deposit charges at the opposite ends of the sample and create a strong, energetically costly depolarization field: $E = -P/\epsilon\epsilon_0 \approx 10^8$ V/m²; here $\epsilon \approx (10 - 100)$ [5, 6] and $P \approx (3 - 7) \times 10^{-2}$ C/m² are the typical permittivity and polarization of the N_F phase. Polydomain textures of thin N_F films that impose no preferred in-plane orientation of \mathbf{P} , such as a film supported by an isotropic fluid

[7, 8] or freely suspended in air [9], present clear evidence of these tendencies. First, the spontaneous polarization is everywhere in the plane of the film, avoiding surface charges, which would occur whenever \mathbf{P} is tilted. Second, the in-plane textures are dominated by two types of domains, in which \mathbf{P} is either uniform or bends into circular vortices, thus avoiding splay deformations and associated space charge in the bulk. Domain walls separating these domains adopt the shapes of conic sections, such as parabolas and hyperbolas [7–9].

The N_F structure changes dramatically when one of the film’s surfaces imposes a unidirectional alignment of \mathbf{P} and the other is azimuthally degenerate. In this case, one might expect a uniform state since circular vortices are not compatible with the unidirectional surface alignment. However, experiments [10] demonstrate that instead of being uniform, the polarization twists around the film normal, so that the vectors \mathbf{P} are antiparallel to each other at the bottom and the top surfaces, thus mitigating the depolarization effect. Since the N_F molecules are not chiral, the film splits into equal-width stripes of alternating twist handedness. An analogous twisting phenomenon was predicted by Khachatryan in 1975 [11] for an infinitely long cylindrical N_F sample, in which \mathbf{P} twists around the axis of the cylinder. In both experiments [10] and in Khachatryan’s model [11], the twisted structures arise from the balance of electrostatic and elastic energies. Clearly, this balance should be af-

* lavrentm@gmail.com

† olavrent@kent.edu

ected by the geometry of confinement (e.g., a film with a large lateral extension or a long cylinder), by surface anchoring at the bounding plates, and by the free ions capable of at least partial screening of bound charges.

In this work, we explore experimentally and theoretically the interplay between electrostatic and elastic energies in the N_F domain structures, taking into account the effects of surface anchoring and ionic screening. The surface anchoring in the experiments is designed to be in-plane apolar, or “bidirectional”, by using a photoalignment technique [12], [13]. There are two reasons: First, apolar anchoring should avoid twists that are artificially created by the antiparallel assembly of two plates with a unidirectional alignment of \mathbf{P} , which happens for mechanically rubbed plates. Second, the photoalignment technique allows one to impose various patterns of surface alignment of \mathbf{P} (including an unwelcome splay), thereby exploring the electrostatics-elasticity balance in different contexts.

We find that, generally, the electrostatic interaction prefers a spatial modulation of \mathbf{P} with a characteristic size λ (e.g., the twist pitch or the domain size), generating an energetic contribution that *increases* with λ . Conversely, any such modulation incurs an elastic or anchoring energy penalty, which *decreases* with λ . Thus, the balance between elastic (or anchoring) energy and the electrostatic interaction generates a preferred value of λ , leading to the various patterns considered here. The two main motifs of these patterns are (i) neighboring domains with a uniform polarization that flips by π when one moves from one domain to the next and (ii) domains with additional left- and right-handed π -twists of polarization along the axis orthogonal to the cell’s plane. As a rule, the first type of pattern occurs in thin (micron) films, while the second pattern is prevalent in thicker slabs.

Note that the nematic director $\hat{\mathbf{n}}$ in the N_F does not have to align with the polarization \mathbf{P} [14]. In this case, we have to consider the flexoelectric coupling (a term proportional to $-(\mathbf{P} \cdot \hat{\mathbf{n}})(\nabla \cdot \hat{\mathbf{n}})$ in the free energy). Such a term, along with a treatment which considers the nematic and polar order separately, can lead to other interesting phases and instabilities in these materials [14–16]. Here, however, we will assume that \mathbf{P} is always parallel to $\hat{\mathbf{n}}$ and $\mathbf{P} \cdot \hat{\mathbf{n}} = \pm P_0$, which occurs when the coupling is sufficiently strong. Our primary interest will be the effects of the uncompensated bound charges at sample boundaries and due to non-vanishing $\nabla \cdot \mathbf{P}$.

The paper is organized as follows: In the next section, we present experimental studies of domain structures in flat slabs with bidirectional anchoring $\hat{\mathbf{n}}_0 = -\hat{\mathbf{n}}_0$ designed to set uniform planar or radial patterns of molecular orientations at the bounding surfaces. The radial pattern produces a topological defect of charge +1. We observe that the N_F avoids monocrystal alignment of \mathbf{P} by forming π -twisted domains (π -TDs) in planar cells, provided they are sufficiently thick (a few microns). The twist axis is perpendicular to the bounding plates. In thin (micron or less) planar cells, the electrostatic en-

ergy is reduced by forming a periodic lattice of elongated “uniform domains” (UDs) with constant \mathbf{P} parallel to $\hat{\mathbf{n}}_0$ but alternating the polarity from one domain to the next. In the radial splay patterns, the surface-imposed divergence of \mathbf{P} is relaxed by the TDs in thick cells and by “pie slices” of splay domains (SDs) in thin cells, with the polarization alternatively pointing toward or away from the defect core.

In the theoretical part (Section III), we first review Khachatryan’s prediction that an unconstrained N_F has a spontaneously twisted polarization \mathbf{P} with a characteristic period λ_z in a cylindrical domain and explore how this period depends on the concentration of ions. We also show that the N_F confined in a planar cell with a bidirectional anchoring will form a π -twist above a critical cell thickness in order to satisfy the anchoring conditions while decreasing the energetic cost of the depolarization field. In Section IV, we consider polarization domain patterns that occur in thin cells with various pre-patterned anchoring conditions. For bidirectional uniform planar anchoring, $\hat{\mathbf{n}}_0 = \text{const}$, striped patterns with a characteristic wavelength λ_x^* emerge. In cells with apolar orientation \mathbf{n}_0 forming a +1 radial “aster” defect, the N_F breaks up into arrays of SDs shaped like “pie slices”. We develop theories for both the stripe width and the number of SD slices. We compare our theoretical predictions and experimental measurements of the number of domain walls (SD slices or stripe widths) in Section V. We draw conclusions and point to future directions in Section VI.

II. EXPERIMENT

A. Materials and methods

We explore an N_F material abbreviated DIO [2] and synthesized in the laboratory as described in [17]. On cooling from the isotropic (I) phase, the phase sequence of DIO is I-174°C-82°C-SmZ_A-66°C- N_F -34°C-crystal, where SmZ_A is an antiferroelectric smectic [18]. The sandwich-type cells are bounded by two glass plates with layers of a photosensitive dye Brilliant Yellow (BY), which shows maximum absorption in the range 400 nm to 550 nm. BY is dissolved in dimethylformamide (DMF) at a concentration 0.5 wt %. The filtered BY-DMF solution is spin-coated onto the substrates at 3000 rpm for 30 seconds and baked for 30 minutes at 90°C. The spin-coating and baking procedures are performed in a humidity-controlled environment with relative humidity fixed at 0.2.

To achieve apolar planar alignment, the BY-coated assembled cell is exposed to a light beam (light source EXFO X-Cite with a spectral range of 320 to 750 nm) with a linear polarizer for 10 minutes. This irradiation induces bidirectional molecular alignment perpendicular to the polarization axis of the normally incident light. The radial aster pattern of the dye molecules at the substrates is induced by irradiating the substrates

through a plasmonic metamask with radial arrangements of nanoslits [12, 13]. The bidirectional apolar anchoring is set by the same light beam that passes through the metamask and acquires local linear polarization orthogonal to the long axis of the nanoslit. The BY molecules realign perpendicularly to the local light polarization, thus the pattern of BY molecules replicates the pattern of nanoslits. To ensure that the surface patterns are the same on the top and bottom plates, these plates are assembled into an empty cell with a preset distance h between them and irradiated by the same light beam. The cell is then filled with DIO in the N phase and then cooled down to the N_F phase.

B. Planar cells

The planar cells in the N and SmZ_A phases show homogeneous textures with the molecular director $\hat{\mathbf{n}}$ parallel to the photoinduced apolar “easy axis” $\hat{\mathbf{n}}_0 = -\hat{\mathbf{n}}_0 = (0, \pm 1, 0)$. Here and in what follows, we use the Cartesian coordinates (x, y, z) in which the y -axis is the direction of the anchoring and the z -axis is normal to the film.

Upon cooling, the texture remain homogeneous for about $(4 - 8)^\circ\text{C}$ below the SmZ_A - N_F transition point, depending on the cell thickness. Thin cells, $h < 2 \mu\text{m}$, preserve uniformity, $\mathbf{P} = P(0, \pm 1, 0)$ for $(6 - 8)^\circ\text{C}$, after which they split into a lattice of UDs elongated along $\hat{\mathbf{n}}_0$, each of width on the order of $10 \mu\text{m}$, Fig. 1(a-d). When $\hat{\mathbf{n}}_0$ is parallel to one of the polarizers, the UDs are practically extinct between two crossed polarizers, Fig. 1(a), and their optical retardance equals that of the optical compensator when the latter is inserted between the sample and the analyzer, Fig. 1(d). The textures observed with polarizers uncrossed counterclockwise, Fig. 1(b), and clockwise, Fig. 1(c), differ little from each other. One concludes that \mathbf{P} in UDs aligns along $\hat{\mathbf{n}}_0$ and their polarity alternates from $\mathbf{P} = P_0(0, 1, 0)$ in one domain to $\mathbf{P} = P_0(0, -1, 0)$ in the next. There are only few regions, marked with a letter “T” in Figs. 1(b,c), in which the textures with uncrossed polarizers do differ, which suggests a twist of \mathbf{P} along the z -axis.

Thick cells, $h > 2 \mu\text{m}$, show a very different behavior. Below 62°C , they develop a stripe pattern of π -twisted domains (π -TDs), recognized by the absence of light extinction when viewed between two crossed polarizers, one of which is along $\hat{\mathbf{n}}_0$, as seen in Fig. 1(e). This N_F texture is similar to the previously studied TDs with alternating left-handed and right-handed twists in cells in which one plate sets a unipolar alignment of \mathbf{P} and the other is azimuthally degenerate [10].

The addition of an ionic salt 1-Butyl-3-methylimidazolium hexafluorophosphate (BMIM-PF₆) suppresses the π -TDs, as the sample is predominantly extinct between the crossed polarizers, Fig. 1(f). The added salt also decreases the temperatures of phase transition by approximately 20°C , in agreement with previous studies [10, 19, 20]. The dependency of a

transmitted light intensity on the angle γ between the directions of polarization of the polarizer and analyzer allows one to determine that the twist angle τ between the bottom and top orientation of \mathbf{P} in the DIO cell of a thickness $h = 4 \mu\text{m}$ is close to 180° , Fig. 1(g-j).

Qualitatively, the observed π -TDs can be understood as the avoidance of a strong depolarization field at the expense of the twist elastic energy and the energy of the domain walls; the balance of these tendencies and the effect of ions will be discussed in Sections III and IV below.

Note that the domain structures presented in Fig. 1 are different from the recently described splay and double-splay domain structures that form in the material RM734 above the phase transition to the N_F [20, 21]. These splay domain structures are optically discernable when the material is exposed to an ionic fluid [20] or an ionic polymer [21]. We also observe the splay domain textures in our RM734 samples doped with BMIM-PF₆, but only above the temperature at which the material transitions into the N_F phase. The splay domains above the N_F temperature range are attributed to the flexoelectric effect, which favors the splay of molecules with head-tail asymmetry [20, 21]. In the N_F phase, this flexoelectricity-triggered splay is suppressed by the space charge that accompanies divergence of \mathbf{P} [20]. As a result, the domain structures in the N_F phase, Fig. 1, are different from the domain structures reported in Refs. [20, 21]. Because of this principal difference, in what follows, we consider only the electrostatic, elastic, and surface anchoring effects and disregard the flexoelectric effect.

C. Radial patterns

The radial pattern of the +1 defect in the N and SmZ_A phases demonstrate smooth splay deformation of the director. In the N_F phase, the textures show domains of two types. The first are “pie-slices”, or splay domains (SDs), with \mathbf{P} parallel or anti-parallel to the radial direction $\hat{\mathbf{r}}$, pointing either away from the core of the +1 defect at $\hat{\mathbf{r}} = 0$ or towards it, as shown in Fig. 2(a,b). As established by polarizing microscopy, within each SD, \mathbf{P} does not twist along the z axis, except perhaps within the domain walls that separate splay sectors of antiparallel \mathbf{P} . These domains are similar to the UDs in the planar cells in the sense that the polarization does not twist. The second type are π -TDs, similar to the π -TDs in the planar cells: \mathbf{P} twists around the z axis by $\tau \approx 180^\circ$, as shown in Fig. 3(a,b).

The frequency of domain appearance depends on the cell thickness and temperature. Thick cells, $h > 6 \mu\text{m}$, upon cooling below 61°C , show exclusively TDs, Fig. 2(e,g). Cells of an intermediate thickness, $1 \mu\text{m} < h < 6 \mu\text{m}$, show both π -TDs and SDs, Fig. 2(e,g). Structures in cells with $h \leq 1 \mu\text{m}$ are either uniformly radial, Fig. 2(h), or show a few SDs. In thin cells, $1 \mu\text{m} < h < 6 \mu\text{m}$, the domains form at about $(5 - 10)^\circ\text{C}$ below the

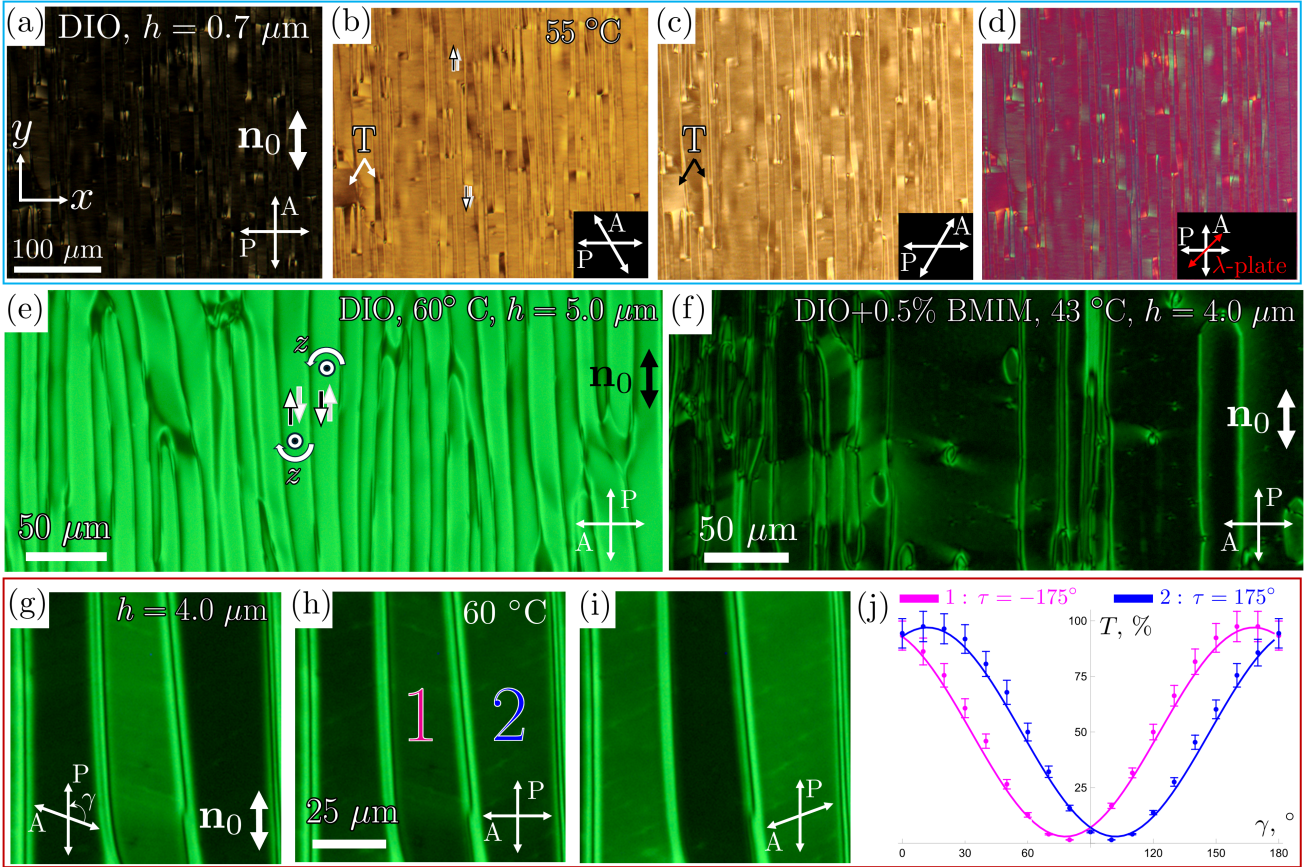


FIG. 1. Domain structures in photoaligned cells with planar apolar anchoring. (a) A polarizing optical microscopy texture of uniform domains (UDs) in a thin N_F cell, $h = 0.7 \mu\text{m}$ (temperature $T = 55^\circ\text{C}$) with bidirectional anchoring indicated by the white double arrow. (b,c) The same, counterclockwise and clockwise uncrossing of analyzer and polarizer, respectively. Pairs of parallel arrows in (b) illustrate that \mathbf{P} does not change along the z -axis normal to the cell but alternates from one UD to the next along the x -axis. (d) The same, observation with an optical compensator; the slow axis is along the red double arrow. (e) A polarizing optical microscopy texture of a thick N_F cell, $h = 5 \mu\text{m}$ ($T = 60^\circ\text{C}$). Light transmission through the cell indicates that the sample is split into π -twisted domains (π -TDs), shown schematically by two antiparallel arrows that twist by π around the z -axis. (f) Domains are suppressed when DIO is doped with 0.5 wt.% of an ionic fluid BMIM-PF₆. (g,h,i) The twisted polarization in the π -TDs is readily recognized by observing the textures with uncrossed (g,i) and crossed (h) polarizers. (j) Fitting the dependence of transmitted light intensity on the angle γ between the polarizers yields the opposite twist angles $\tau = \pm 175^\circ$ for the two domains highlighted in (h). Textures (e-i) are captured using a green interferometric filter with a center wavelength $\lambda = 532 \text{ nm}$ and bandwidth of 1 nm.

SmZ_A-N_F transition point. The thickness dependency of the temperature at which the domains appear can be qualitatively explained by the temperature dependence of the polarization magnitude P_0 which increases from about $P_0 = 3.4 \times 10^{-2} \text{ C/m}^2$ to $P_0 = 4.6 \times 10^{-2} \text{ C/m}^2$ [2] as the temperature decreases following the SmZ_A-N_F transition; the bound charge effects leading to the domains might be weaker than the stabilizing surface anchoring and ion screening.

Within the range of coexistence, the fraction of the SD domains increases as the cell thickness h decreases, Fig. 2(e,g). The number of domains increases with the cooling rate, Fig. 2(c,d), which is natural as the higher cooling rate does not leave time for the domains to coalesce and bring the system closer to the equilibrium. Another potential reason is that for a longer cooling time, the highly polar material absorbs ions from the

surroundings, such as glue, BY layer, etc., to screen the bound charge $\rho = -\nabla \cdot \mathbf{P}$. The ion concentration of free ions in the N_F cannot be measured directly by conventional techniques since the polarization reorientation reduces the electric field in the N_F bulk to zero [22]. Some support of the idea that the concentration of ions can increase with time is provided by measurement in the N phase, by briefly heating the sample to 120°C ; the concentration is found to increase from $c(0) = 5.0 \times 10^{22} \text{ ions/m}^3$ at the start of experiment to $c(18 \text{ hours}) = 6.3 \times 10^{22} \text{ ions/m}^3$ after 18 hours of keeping the sample in the N_F phase at 65°C .

The number of domains decreases significantly when DIO is doped with the ionic fluid BMIM-PF₆, Fig. 4. At a weight concentration 0.5 wt % of BMIM-PF₆, which corresponds to the concentration of ions $1.5 \times 10^{25} \text{ ions/m}^3$ when added molecules are fully ionized,

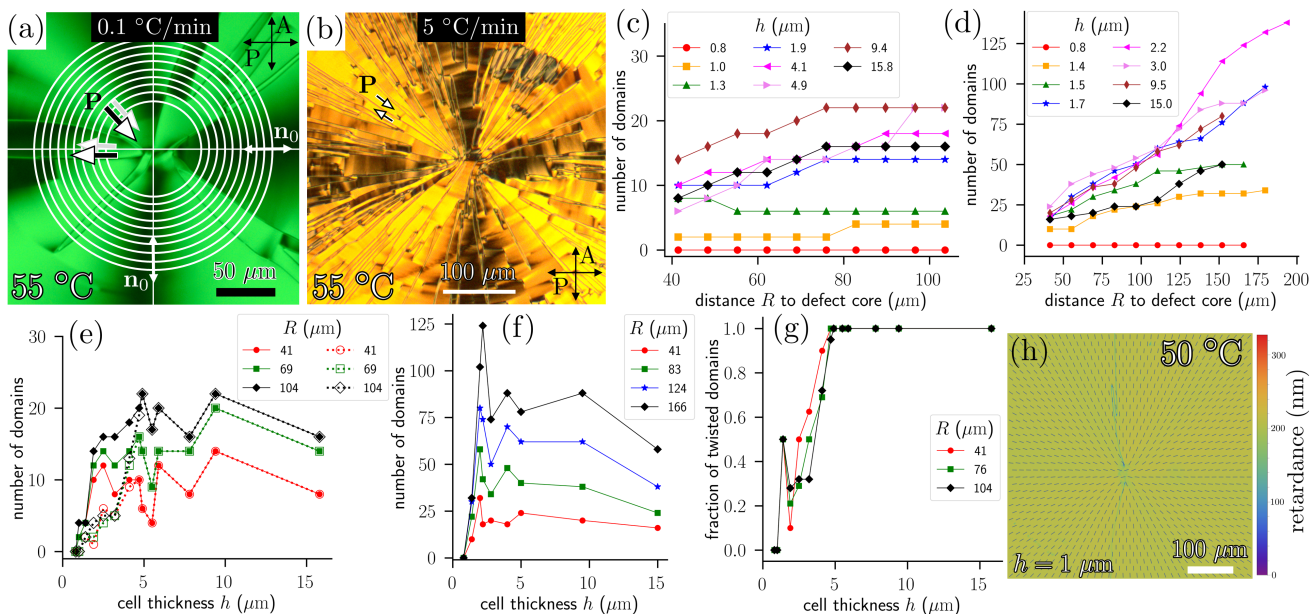


FIG. 2. Structure of a +1 radial prepatterned splay defect. (a) A polarizing optical microscopy texture (recorded in a monochromatic light using a green filter with 532 nm wavelength and 1 nm bandwidth) of an N_F cell with thickness $h = 2 \mu\text{m}$, $T = 55^\circ\text{C}$, and cooling rate $0.1^\circ\text{C}/\text{min}$. The parallel arrows show that the polarization at the bottom and top plates are parallel to each other, but alternate from one splay domain (SD) to the next along the azimuthal direction in the xy plane. (b) Similar cell, $h = 2 \mu\text{m}$, cooling rate $5^\circ\text{C}/\text{min}$. (c,d) Number of domains as a function of distance R from the defect core for cell thicknesses $h = (1 - 16) \mu\text{m}$, cooling rates 0.1°C and 5°C , respectively. (e) Number of domains vs h measured at different distances R from the defect core, cooling rate $0.1^\circ\text{C}/\text{min}$. Filled symbols and solid lines correspond to the total number of domains, while open symbols and dashed lines correspond to π -TDs. (f) The thickness dependence of the number of domains, cooling rate $5^\circ\text{C}/\text{min}$. (g) Fraction of TDs as a function of the cell thickness h measured at different distances R from the defect core; cooling rate $0.1^\circ\text{C}/\text{min}$. (h) Radial structure with no domains in a thin cell, $h = 1 \mu\text{m}$, imaged using the Microimager PolScope with the ticks showing the director field $\hat{\mathbf{n}}(x, y)$.

the N_F phase preserves its ferroelectric ordering, as reported by Zhong et al. [19]. The free ions screen the space charges created by the splay of polarization and help to minimize the electrostatic energy.

III. SPONTANEOUS P TWIST

To begin the theoretical analysis, it is worth to first review Khachatryan's theoretical prediction from 1975 [11] that N_F s in an infinite sample (thick film) may spontaneously develop *twisted* polarization \mathbf{P} domains of linear size R with a characteristic wavelength λ_z . Experiments on thin films [10] provide qualitative support of this prediction.

A. Twist in a cylinder

We will consider a cylindrical domain with radius R and length h , as shown in Fig. 5. The intuitive explanation is that, in the absence of twist, a uniform polarization ($\mathbf{P} = P_0\hat{\mathbf{x}}$, say) will generate a strong depolarization field due to the accumulation of uncompensated charge on the domain boundary, as shown on the left panel of Fig. 5. The charges can be partially compen-

sated by *twisting* the direction of \mathbf{P} along the cylinder, as demonstrated on the right panel of Fig. 5. We can calculate the optimal period λ_z of the twist by balancing this electrostatic energy gain with the elastic cost of the deformation. To be more specific, the N_F has a continuously varying polarization vector $\mathbf{P} \equiv \mathbf{P}(\mathbf{r}) = P_0\mathbf{n}(\mathbf{r})$ within the material, with some fixed magnitude $|\mathbf{P}| = P_0$ and a varying orientation $\mathbf{n}(\mathbf{r})$. Spatial variations in \mathbf{P} or domain boundaries will generate a bound charge distribution given by $\rho = -\nabla \cdot \mathbf{P}$. This distribution of charge is energetically costly and we can calculate the corresponding (screened) electrostatic energy as

$$F_\rho = \frac{1}{8\pi\epsilon\epsilon_0} \iint \frac{\rho(\mathbf{r})\rho(\mathbf{r}')e^{-\kappa|\mathbf{r}-\mathbf{r}'|}}{|\mathbf{r}-\mathbf{r}'|} d\mathbf{r}' d\mathbf{r}, \quad (1)$$

where ϵ is the relative dielectric constant of the material and $\kappa \equiv 1/\lambda_D$ is the (inverse) Debye screening length. The screening comes from the free ions present in the material, with $\kappa \approx \sqrt{n}e/\sqrt{\epsilon\epsilon_0 k_B T}$ for monovalent ions with concentration n , with e the fundamental charge, $\epsilon\epsilon_0$ the material permittivity, and $k_B T$ the thermal energy. This free energy F_ρ can be expressed in Fourier space as

$$F_\rho = \frac{1}{2\epsilon\epsilon_0} \int \frac{|\mathbf{k} \cdot \tilde{\mathbf{P}}_{\mathbf{k}}|^2}{|\mathbf{k}|^2 + \kappa^2} \frac{d\mathbf{k}}{(2\pi)^3}, \quad (2)$$

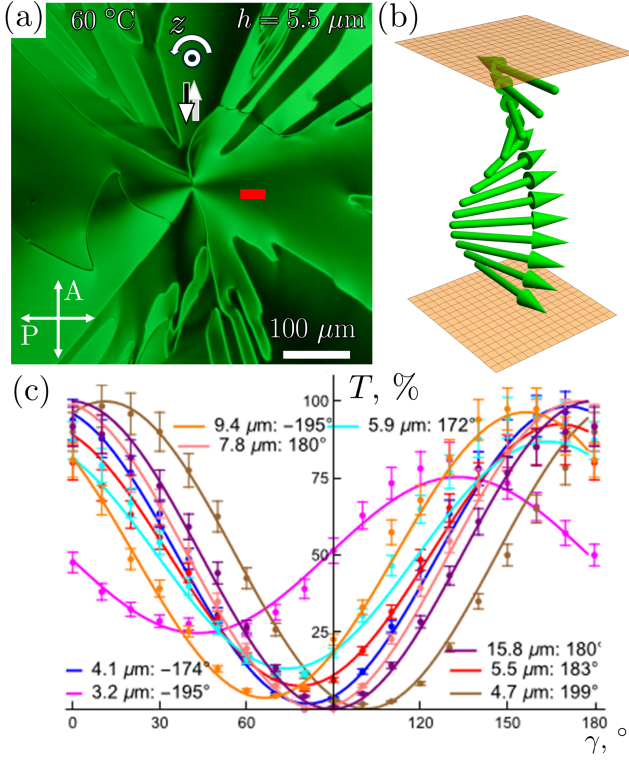


FIG. 3. Structure of a +1 radial prepatterned splay defect. (a) A polarizing optical microscopy texture (recorded in a monochromatic light using a green filter with 532 nm wavelength and 1 nm bandwidth) of an N_F in a cell of the thickness $h = 5.5 \mu\text{m}$ (DIO, temperature $T = 60^\circ\text{C}$). (b) Fitting the dependence of transmitted light intensity on the angle γ between the polarizers yields the twist angle $\tau \approx 180^\circ$ for samples of different thickness in the range $3 \mu\text{m} < h < 16 \mu\text{m}$.

where $\tilde{\mathbf{P}}_{\mathbf{k}} \equiv \int d\mathbf{r} e^{-i\mathbf{k}\cdot\mathbf{r}} \mathbf{P}(\mathbf{r})$. Note that even in cases where $\rho(\mathbf{r})$ vanishes in the bulk of a sample or domain, we may still get contributions to F_ρ due to uncompensated charges at the boundaries (the depolarization field).

Spatial variations of \mathbf{P} will incur elastic energy penalties. The (nematic) elastic energy is given by the Frank form

$$F_n = \int d\mathbf{r} \left[\frac{K_1}{2} (\nabla \cdot \mathbf{n})^2 + \frac{K_2}{2} (\mathbf{n} \cdot (\nabla \times \mathbf{n}))^2 + \frac{K_3}{2} (\mathbf{n} \times (\nabla \times \mathbf{n}))^2 \right], \quad (3)$$

with K_1 , K_2 , and K_3 the splay, twist, and bend elastic constants, respectively [23]. To see how F_n and F_ρ compete to create variations in \mathbf{P} , we look for free energy minimizers which only vary along the vertical direction z :

$$\mathbf{P} = P_0 (\cos[\phi(z)], \sin[\phi(z)], 0) \Theta(x, y), \quad (4)$$

where $0 \leq z \leq h$, $\phi(z)$ is the polar angle of the \mathbf{P} orientation, and $\Theta(x, y) = 1$ whenever $x^2 + y^2 \leq R$ and $\Theta(x, y) = 0$ otherwise. This means that we expect to have uncompensated charges at the cylinder boundary,

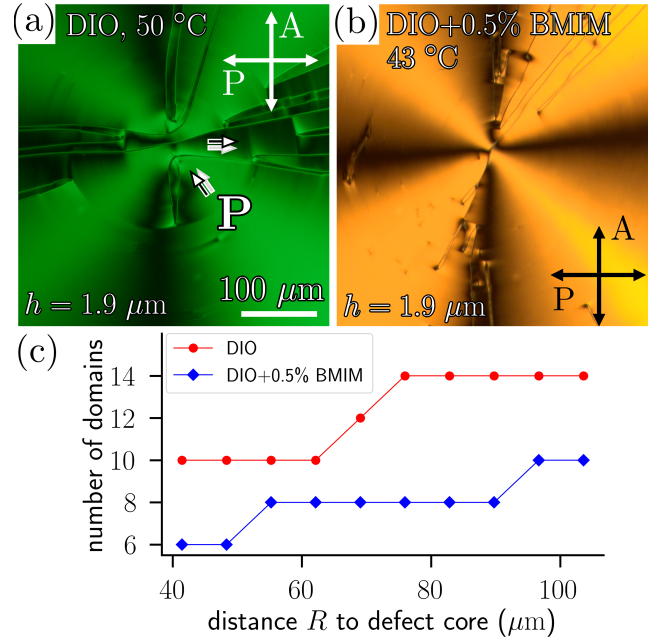


FIG. 4. A polarizing optical microscopy texture (recorded in a monochromatic light using a green filter with 532 nm wavelength and 1 nm bandwidth) of the N_F phase of (a) pure DIO, $T = 50^\circ\text{C}$ and (b) DIO doped with BMIM-PF₆, $T = 43^\circ\text{C}$ in cells with radial patterns of the thickness $h = 1.9 \mu\text{m}$. (c) Number of domains versus distance to the +1 defect center for pure DIO and DIO doped with BMIM-PF₆.

as shown in Fig. 5. We now assume without loss of generality that the angle $\phi(z)$ is a periodic function with some period $2\pi/k_z$ which might tend toward infinity:

$$\phi(z) = k_z z + \psi(z), \quad (5)$$

where $\psi(z) = \psi(z + 2\pi/k_z)$. We may expand the phase factor associated with this angle as

$$e^{i\phi(z)} = e^{ik_z z} \sum_{m=-\infty}^{\infty} A_m e^{ik_z m z}, \quad (6)$$

where A_m are complex Fourier coefficients satisfying

$$\sum_{m=-\infty}^{\infty} A_m A_{m-n}^* = \begin{cases} 1 & n = 0 \\ 0 & n \neq 0 \end{cases}. \quad (7)$$

Provided we have a thick sample with $h \gg \lambda_D$, we substitute Eqs. (4,6) into Eq. (2) and find that

$$F_\rho = \frac{\pi P_0^2 R^2 h}{2\epsilon\epsilon_0} \sum_{n=-\infty}^{\infty} I_1(\alpha_n) K_1(\alpha_n) [A_n^2 + (A_n^*)^2], \quad (8)$$

where $\alpha_n \equiv R\sqrt{[k_z(n+1)]^2 + \kappa^2}$ and $I_1(\alpha)$, $K_1(\alpha)$ are the modified Bessel functions of the first and second kind, respectively. It is worth noting that $I_1(\alpha)K_1(\alpha)$ is a monotonically *decreasing* function of α , meaning that the electrostatic energy favors *large* values of $\alpha_n \sim k_z$. As we shall see, the elastic contribution will favor small values of k_z , instead.

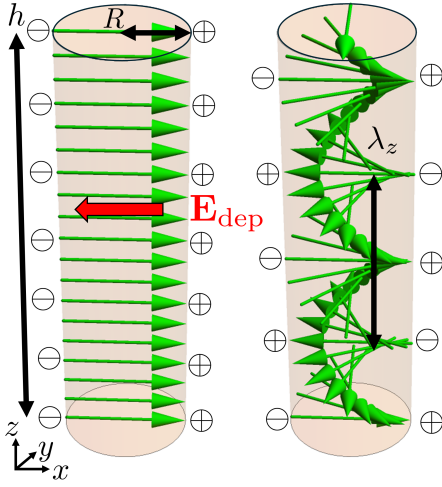


FIG. 5. A cylindrical domain with uniform polarization $\mathbf{P} = P_0 \hat{\mathbf{x}}$ (left panel) incurs an energetic cost due to the uncompensated charges and consequent depolarization field \mathbf{E}_{dep} . Instead, the polarization \mathbf{P} can *twist* (right panel) with a certain period λ_z and create regions of alternating charge, thereby partially mitigating the energetic cost of the depolarization field. This twist is balanced by the elastic cost of the twist.

Given the ansatz in Eq. (4) and ignoring any elastic deformation or anchoring energy at the cylinder boundary, only the *twist* term proportional to K_2 contributes to the elasticity and we find

$$F_n = \frac{\pi K_2 k_z^2 R^2 h}{2} + \frac{\pi K_2 R^2 h}{2\lambda_z} \int_0^{\lambda_z} dz \left(\frac{d\psi}{dz} \right)^2. \quad (9)$$

We may now move to Fourier space by making use of the expansion in Eqs. (6,7). We find that

$$F_n = \frac{\pi R^2 h K_2 k_z^2}{2} \left[1 + \sum_{n=-\infty}^{\infty} n^2 |A_n|^2 \right], \quad (10)$$

which clearly is minimized for $k_z \rightarrow 0$. We can also see that higher order modes A_n with $|n| > 0$ always cost more elastic energy. This is less obvious for the electrostatic interaction in Eq. (8), but it is possible to argue on more general grounds [11] that there is a stable free energy minimum with $A_n = 0$ for all $|n| > 0$.

Looking at solutions with just the $n = 0$ mode, we find that the total free energy is given by

$$F = F_n + F_\rho = \frac{\pi R^2 h}{2} \left[\frac{P_0^2 I_1(\alpha_0) K_1(\alpha_0)}{\epsilon \epsilon_0} + K_2 k_z^2 \right], \quad (11)$$

where $\alpha_0 = R\sqrt{k_z^2 + \kappa^2}$ and we recognize that with just the single mode we must have $\sum_n |A_n|^2 = A_0^2 = (A_0^*)^2 = 1$ from Eq. (7). The total free energy in Eq. (11) now can be minimized with respect to k_z . We look for solutions for large domain size R such that $R/\lambda_D \gg 1$. In this case, $\alpha_0 \gg 1$ and we can make use of the asymptotic expansion $I_1(\alpha_0) K_1(\alpha_0) \approx (2\alpha_0)^{-1}$. We find a minimum

free energy at $k_z = k_z^*$, which corresponds to a preferred pitch $\lambda_z = 2\pi/k_z^*$ of

$$\lambda_z = 2\pi \left[\frac{P_0^{4/3}}{(4K_2 R \epsilon \epsilon_0)^{2/3}} - \kappa^2 \right]^{-1/2}. \quad (12)$$

Substituting in reasonable values $\epsilon = 100$, $P_0 \approx 4.4 \times 10^{-2}$ C/m², $K_2 = 5$ pN, $R = 50$ μ m, and $T = 350$ K, and assuming no screening ($\kappa = 0$) we find a pitch of $\lambda_z^* \approx 0.5$ μ m. This result is consistent with the previously reported data [10] and with Fig. 1.

The pitch in Eq. (12) is analogous to the result derived by Khachatryan [11], with some key corrections involving the contributions of screening. This result, along with the correction, was also recently found by Paik and Selinger using a different analysis [15]. We see that we get the twisted structure only when the screening is sufficiently weak: $\lambda_D^2 > (4K_2 R \epsilon \epsilon_0)^{2/3} P_0^{-4/3}$. Assuming that the screening comes from some concentration c of monovalent ions, then we have the squared Debye screening length $\lambda_D^2 = \kappa^{-2} = \epsilon \epsilon_0 k_B T / (c e^2)$. The twisted state occurs only when the concentration of ions is below some critical value:

$$c < c^* = \frac{(\epsilon \epsilon_0)^{1/3} k_B T P_0^{4/3}}{(4K_2 R)^{2/3} e^2}. \quad (13)$$

We find that, given the reasonable parameters mentioned above and $T = 350$ K, $c^* \approx 3 \times 10^{22}$ ions/m³, which is on the same order of magnitude as the concentration of ions measured in the N phase, $c = (5 - 6) \times 10^{22}$ ions/m³, at which the TD domains are observed, Fig. 1(a, c-f). However, the experimental data obtained in the N phase might not be representative of the concentration of ions in the N_F phase. Nevertheless, the theoretical estimate appears to be consistent with the experiments in which the TDs disappear when DIO is doped with the ionic fluid BMIM-PF₆ [see Fig. 1(b)], which could potentially increase the concentration of ions by orders of magnitude.

B. π -twists

We have so far considered thick cells with the polarization \mathbf{P} twisting in a cylinder along the direction normal to the cell (the z -axis). In this case, the elastic and electrostatic energies compete throughout the bulk of the sample. However, we now consider an N_F confined to a *thin* cell with boundary conditions, such as a certain imposed nematic orientation \mathbf{n}_0 at the top and bottom of the cell, as in the samples shown in Fig. 1. When the anchoring is strong, the sample thickness h will typically set the periodicity of the twist along the z direction. This is demonstrated by polarizing light microscopy (see [7] for details) in Fig. 1(c-f), which shows that most domains in the cells exhibit a π -twist in the polarization \mathbf{P} from the bottom to the top surface.

However, for even thinner cells, the π -twist becomes too energetically costly. Indeed, there is a critical thickness h^* for which we get twisted domains if $h > h^*$ and domains with uniform \mathbf{P} orientation for $h < h^*$. We can calculate the critical thickness h^* by considering a simple square domain with dimension L in the cell of thickness t . At sufficiently large anchoring strengths, we may assume that \mathbf{P} remains in the xy plane and that \mathbf{P} runs along $\hat{\mathbf{y}}$ on the top and bottom surfaces. We compare two polarization configurations: a uniform $\mathbf{P}_{\text{uniform}} = P_0 \hat{\mathbf{y}}$ and a π -twisted $\mathbf{P}_{\pi\text{-twist}} = P_0 \sin(\pi z/h) \hat{\mathbf{x}} + P_0 \cos(\pi z/h) \hat{\mathbf{y}}$, with both vanishing outside of the region $-L/2 < x, y < L/2$ and $0 < z < h$. The Fourier transforms are

$$\begin{cases} \tilde{\mathbf{P}}_{\text{uniform}} = \frac{8P_0 e^{-ihk_z/2} \sin(\frac{k_x L}{2}) \sin(\frac{k_y L}{2}) \sin(\frac{k_z L}{2}) \hat{\mathbf{y}}}{k_x k_y [\pi^2 - h^2 k_z^2] e^{\frac{ihk_z}{2}}} \\ \tilde{\mathbf{P}}_{\pi\text{-twist}} = \frac{8P_0 \sin(\frac{k_x L}{2}) \sin(\frac{k_y L}{2}) \cos(\frac{hk_z}{2}) [\pi \hat{\mathbf{x}} + ihk_z \hat{\mathbf{y}}]}{k_x k_y [\pi^2 - h^2 k_z^2] e^{\frac{ihk_z}{2}}} \end{cases} \quad (14)$$

Substituting these transforms into Eq. (2) and assuming that $L\kappa \gg 1$ (strong screening or large sample size) yields the dipolar energy

$$F_\rho = \begin{cases} \frac{LhP_0^2}{\epsilon\epsilon_0\kappa} & \text{for } \tilde{\mathbf{P}}_{\text{uniform}} \\ \frac{LhP_0^2}{4\epsilon\epsilon_0\kappa} & \text{for } \tilde{\mathbf{P}}_{\pi\text{-twist}} \end{cases} \quad (15)$$

The electrostatic energy cost of the polarization configuration gets a four-fold decrease from the π -twist along the z -axis.

The π -twisted configuration incurs an elastic energy penalty given by $F_n = K_2 L^2 \pi^2 / (2h)$, which follows from substituting $\mathbf{n}_{\text{twist}} = \sin(\pi z/h) \hat{\mathbf{x}} + \cos(\pi z/h) \hat{\mathbf{y}}$ into the Frank free energy, Eq. (3). The elastic energy decreases with cell thickness h , while the dipolar energy in Eq. (15) increases. The balance yields a critical thickness

$$h^* = \sqrt{\frac{2\epsilon\epsilon_0\kappa K_2 L \pi^2}{3P_0^2}}. \quad (16)$$

The critical thickness h^* increases with the domain size L because the dipolar energy comes from uncompensated charge at the boundary of the domain. However, even for extremely large domains with $L \approx 1$ mm, we find a remarkably small $h^* \approx 1 - 10 \mu\text{m}$ for the experimental conditions considered here (assuming $\lambda_D = \kappa^{-1} \approx 0.1 - 10 \mu\text{m}$). In other words, the depolarization field plays a significant role even though it is essentially a boundary effect. We expect to see π -twisted domains, such as those shown in Fig. 1(a,c-f), even for cells with micron-scale thickness h . In the experiments, we find that essentially all domains are twisted for thicknesses $h > 2 \mu\text{m}$, consistent with this result.

Confinement can induce chirality (twist) in solid state ferroelectrics, as well, especially in nanostructured materials [24, 25], although intrinsically chiral solid ferroelectrics are also possible. As we shall see in the next section, the polarization can also be modulated in the perpendicular direction (along the cell boundary).

Such modulated states exist in the solid state [25], even with smooth variation of the polarization direction. We will thus draw some additional comparisons between the crystalline and nematic ferroelectrics in the following.

IV. DOMAIN PATTERNS

Apart from the π -twist along the z direction, we know that the N_F in these thin cells breaks up into domains along the cell surface. We will study some prototypical cases, including the stripes in Fig. 1 and the pie slices in Figs. 2,3. Let us begin with an analysis of the stripes in Fig. 1.

A. Stripe domains

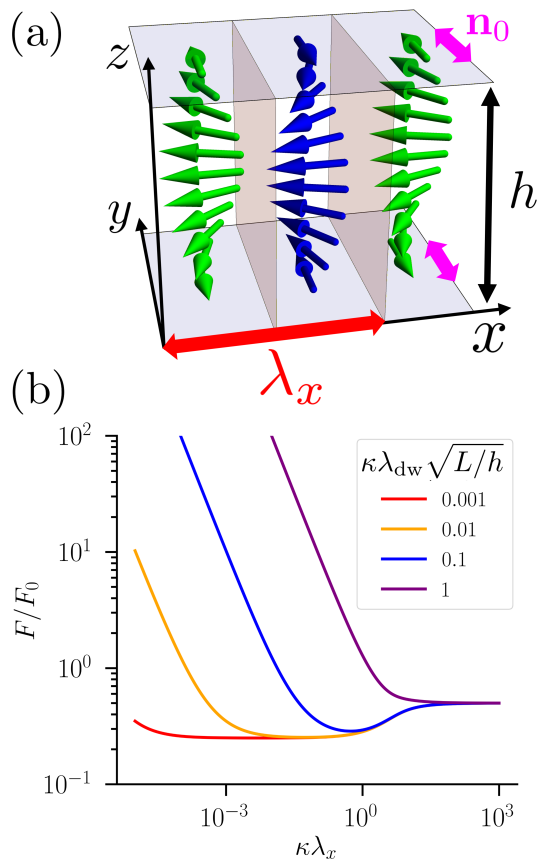


FIG. 6. (a) Schematic of a possible polarization direction in the striped domains with characteristic wavelength λ_x , with the anchoring nematic direction \mathbf{n}_0 on the top and bottom surfaces. (b) Dimensionless energy [Eq. (20)] of the striped domain configuration, taking into account both the electrostatic energy contribution and the energy of domain walls. We see that there is a minimum at a certain $\kappa\lambda_x$, indicating that the striped configuration is favorable. We show the energy for various values of the dimensionless parameter $\kappa\lambda_{\text{dw}}\sqrt{L/h}$ discussed in the text.

The domains observed in Fig. 1 are reminiscent of

structures found in thin films of solid, uniaxial ferroic materials [26], where the polarization \mathbf{P} (or magnetization for ferromagnets) forms stripes of alternating orientation (although the polarization typically has components perpendicular to the film surface, unlike the N_F which has \mathbf{P} parallel to the xy plane) [27, 28]. Like the domains in the N_F and the cylindrical case considered above (see Fig. 5), the stripes in solid ferroics are generated to mitigate the strong depolarization field [29, 30]: A thick stripe will break up into thinner stripes in order to create more cancellation of the uncompensated charge at the stripe boundaries. Similar striped patterns appear in ferromagnetic crystals, with the patterns analyzed 90 years ago by Landau and Lifshits [31].

Consider a thin, square cell with thickness h and square cross section with area $A_{xy} = L^2$, where $L = L_x = L_y$ is the linear extent of our sample. The basic idea, also discussed in detail by Kittel for solid ferromagnetic materials [32], is that the dipolar energy density $f_\rho = F_\rho/A_{xy}$ per area of the cell will scale approximately as $f_\rho \propto \lambda_x$, with λ_x the stripe size for stripes running along the y -axis, say. Meanwhile, the introduction of alternating domains of \mathbf{P} will incur a cost due to the domain walls. There will be approximately $2L/\lambda_x$ domain walls in the sample, so the associated free energy density will scale according to $f_{\text{dw}} \propto 1/\lambda_x$. We see, therefore, that there should be an optimal value of λ_x which balances the two energies f_{dw} and f_ρ .

Let us analyze the optimal wavelength λ_x by assuming that we have very strong anchoring so that within each stripe we have a uniform π -twisted polar-

ization $\mathbf{P} = \pm \mathbf{P}_{\pi\text{-twist}}$ which satisfies the bidirectional boundary conditions at the cell surface, as illustrated in Fig. 6(a). Between each stripe domain at the cell surfaces, we have a 180° flip in the polarization orientation. One possibility, illustrated in Fig. 6(a), is that adjacent domains are of opposite chirality, so that the polarization field is uniform in the middle of the cell at $z = h/2$. The corresponding polarization field $\mathbf{P}_{\text{stripe}}$ for this configuration reads

$$\mathbf{P}_{\text{stripe}} = \frac{4P_0}{\pi} \sum_{n=1}^{\infty} \frac{1}{n} \sin\left(\frac{\pi n}{2}\right) \cos(nq_x x) \cos\left(\frac{\pi z}{h}\right) \hat{y} + P_0 \sin\left(\frac{\pi z}{h}\right) \hat{x}, \quad (17)$$

where $q_x = 2\pi/\lambda_x$ is the wavevector associated with the stripe wavelength λ_x [see red double arrow in Fig. 6(a)]. The summation over n is the mode expansion of a square wave, so that we have a rapid reorientation of \mathbf{P} from $+P_0\hat{y}$ to $-P_0\hat{y}$ at the top and bottom of the cell ($z = 0, h$), as illustrated in Fig. 6(a). Let us assume that the striped configuration has some lateral extent $0 < x, y < L$, respectively. For simplicity, we also assume that the total sample is neutral, which means that L should be some integer multiple of λ_x .

We substitute the Fourier-transformed Eq. (17) into Eq. (2) to find the dipolar energy of this configuration. Much like the cylinder domain considered previously, we expect that the electrostatic energy will increase with increasing λ_x , as larger λ_x means that we have more uncompensated charge at the boundaries of the stripes. We find, for large sample sizes $L\kappa \gg 1$, that

$$F_\rho = \frac{4P_0^2}{\pi^3 \epsilon \epsilon_0} \iiint_{-\infty}^{\infty} \frac{\cos^2\left(\frac{z}{2}\right) \sin^2\left(\frac{xL}{2h}\right) \sin^2\left(\frac{yL}{2h}\right)}{(x^2 + y^2 + z^2 + h^2\kappa^2)(\pi^2 - z^2)^2} \left[\frac{16x^2 z^2}{\pi^2 h} \left[\sum_{n=1}^{\infty} \frac{h^2 \lambda_x^2 \sin\left(\frac{\pi n}{2}\right)}{n(\lambda_x^2 x^2 - 4\pi^2 n^2 h^2)} \right]^2 + \frac{h^3 \pi^2}{y^2} \right] dx dy dz \quad (18)$$

$$\approx \frac{h^2 L P_0^2}{\pi^3 \epsilon \epsilon_0} \left[\int_{-\infty}^{\infty} dz \frac{\cos^2\left(\frac{z}{2}\right) \pi^4}{[\pi^2 - z^2]^2 \sqrt{z^2 + h^2\kappa^2}} + \frac{2\pi\lambda_x}{h} \sum_{n=1}^{\infty} \frac{\sin^2\left(\frac{\pi n}{2}\right)}{n^2 \sqrt{(2\pi n)^2 + (\kappa\lambda_x)^2}} \right]. \quad (19)$$

As long as the screening contribution in the sum in Eq. (19) is negligible, then the electrostatic energy F_ρ grows with λ_x . (We expect this to happen whenever the equilibrium λ_x satisfies $\lambda_x \kappa \lesssim 1$.) So, the electrostatic energy prefers to have a small λ_x . However, decreasing λ_x will introduce more domain walls into the system.

The nature of the domain walls may be complex due to the twist in the polarization \mathbf{P} . Experiments indicate that the domain wall may consist of surface disclination lines. These lines come in pairs, as the polarization is uniform at $z = h/2$ [4, 33, 34]. An estimate for the energy of the wall (per unit length) would be $f_\pi^{\text{disc}} \approx 2K$, with K an elastic constant. Another possibility is that the domain wall is a solitonic, Bloch wall structure, which we may call a π -wall as \mathbf{P} flips by 180° across

the wall [7]. The energy per unit length of one such π -wall is given by $f_\pi^{\text{wall}} = 2\sqrt{2KhW}$, where K is an elastic constant, W is the anchoring strength, and h is the cell thickness. The total elastic cost of domain walls is thus approximately $F_{\text{dw}} \approx 2f_\pi L^2/\lambda_x$, with f_π either the solitonic wall (f_π^{wall}) or disclination line pair (f_π^{disc}) energy density.

Putting it all together, the total energy $F = F_\rho + F_{\text{dw}}$ of a striped domain configuration reads

$$\frac{F}{F_0} = \frac{1}{4} + \frac{\kappa\lambda_x}{\pi^2} \sum_{n=1}^{\infty} \frac{[1 - (-1)^n]}{n^2 \sqrt{(2\pi n)^2 + (\kappa\lambda_x)^2}} + \frac{(\kappa\lambda_{\text{dw}})^2 L}{\kappa\lambda_x h} \approx \frac{1}{4} + \frac{2\kappa\lambda_x}{\pi^2 \sqrt{4\pi^2 + (\kappa\lambda_x)^2}} + \frac{(\kappa\lambda_{\text{dw}})^2 L_y}{\kappa\lambda_x h}, \quad (20)$$

where $F_0 = hP_0^2 L(\epsilon\epsilon_0\kappa)^{-1}$ is a characteristic free energy and $\lambda_{\text{dw}} = (2f_\pi\epsilon\epsilon_0)^{1/2}P_0^{-1}$ is a characteristic length associated with the domain wall. Note that the length λ_{dw} is quite small (on the order of nanometers) and arises from the interplay between the elastic cost of domain walls and the electrostatics. A similar length was derived some time ago by balancing analogous energetic contributions [35]. We have made an additional assumption that we can take $h\kappa \gg 1$ in the left-over integration in Eq. (19), which will not change the location of the minimum of F with respect to λ_x , which we will now explore.

We plot the dimensionless free energy F/F_0 in Eq. (20) versus $\kappa\lambda_x$ in Fig. 6(b) for various values of $\kappa\lambda_{\text{dw}}\sqrt{L/h}$, with L the linear extent of the sample. It is possible to numerically minimize the function in Eq. (20), which demonstrates that for $\kappa\lambda_{\text{dw}}\sqrt{L/h} < 0.618$, the free energy curve has a global minimum at a finite value of λ_x , indicating that the system prefers to make stripes of a certain size. For larger values, the free energy minimum corresponds to $\lambda_x \rightarrow \infty$ and a uniform polarization state. In the low screening limit $\kappa\lambda_{\text{dw}} \ll \sqrt{h/L}$, the preferred wavelength (free energy minimum) is at, approximately,

$$\lambda_x^* \approx 5.4\lambda_{\text{dw}}\sqrt{\frac{L}{h}}. \quad (21)$$

B. Pie slice domains

We now consider the +1 aster defect anchoring condition, with $\mathbf{n}_0 = \hat{\mathbf{r}}$ the preferred orientation at the top and bottom cell surfaces. A pure +1 aster defect in the polarization vector, $\mathbf{P} = P_0\hat{\mathbf{r}}$, has a corresponding charge density distribution

$$\rho(r) = -\nabla \cdot \mathbf{P} = -\frac{P_0}{r}. \quad (22)$$

Note that the charge is no longer confined to the boundary, as in the situations considered previously (the cylindrical and striped domains). Instead, there is a distribution of bound charge concentrated at the origin of the defect. Like the boundary charges, this charge is energetically costly, so the N_F prefers to reorient along the $\hat{\boldsymbol{\theta}}$ direction to create a net neutral charge configuration, forming a series of n_θ pairs of alternating \mathbf{P} domains (with $\mathbf{P} \parallel \pm\hat{\mathbf{r}}$), as shown in Fig. 7(a). Of course, we also expect a π -twist along the z -direction, but we will neglect the z -dependence for simplicity, focusing on the regions of the N_F near the cell surface, where \mathbf{P} is forced parallel to the radial direction due to anchoring conditions.

So, consider the polarization \mathbf{P} configuration in a circular domain of radius R , confined to a cell with thickness h . Far from the defect, as $R \rightarrow \infty$, we expect to see striped domains with the preferred wavelength λ_x^* calculated in the previous section. However, near the defect, we expect the bound charge distribution in the

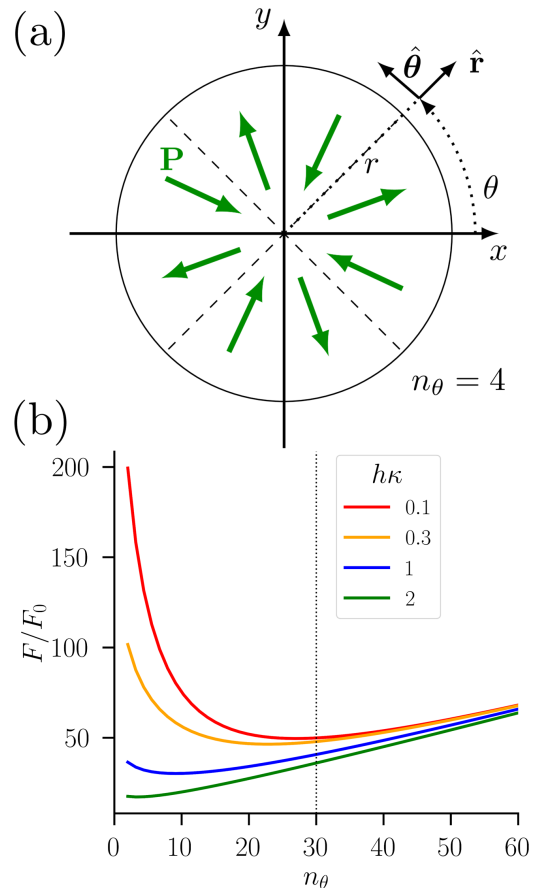


FIG. 7. (a) Schematic of the polarization orientation near the cell surface for a cell pre-patterned with a +1 defect. Apart from the domain walls (along the x and y axes and along the dashed line), the polarization \mathbf{P} runs along the radial direction $\hat{\mathbf{r}}$. The polarization configuration has $n_\theta = 4$ pairs of “pie-slice” sectors of anti-parallel \mathbf{P} . (b) Plot of the rescaled free energy F/F_0 in Eq. (27) of a pie-slice pattern with n_θ cuts for various values of $h\kappa$, with κ the inverse Debye screening length and h the cell thickness. We fix $R/h = 100$ and $\eta_0 = 30$. We see that the Coulomb and elastic energies balance to generate an optimal value of n_θ (the free energy minimum). The dashed vertical line indicates the optimal value in the low screening $\kappa \rightarrow 0$ limit.

bulk should play a more significant role. We see in experiments that the sample breaks up into “pie slice” domains with sharp tips, as shown in Fig. 7(a,b). Assuming the polarization remains in the xy plane and does not depend on the distance r from the defect, the form of the polarization vector of such a configuration is

$$\mathbf{P} = P_0 \cos[\phi(\theta)]\hat{\mathbf{r}} + P_0 \sin[\phi(\theta)]\hat{\boldsymbol{\theta}}, \quad (23)$$

where $\phi(\theta)$ describes the polarization orientation away from the $\hat{\mathbf{r}}$ direction. The bound charge distribution due to this polarization \mathbf{P} is

$$\rho(r, \theta) \approx -\frac{P_0 \cos[\phi(\theta)]}{r}, \quad (24)$$

where we have assumed that $\partial_\theta \phi \ll 1$ is negligibly small throughout most of the sample. Regions of opposite

(cancelling) charge are created by alternating between $\phi(\theta) = 0, \pi$, corresponding to \mathbf{P} parallel or anti-parallel, respectively, to $\hat{\mathbf{r}}$.

We consider a single-mode approximation so that $\cos[\phi(\theta)] \approx \cos(n_\theta\theta)$ and $2n_\theta$ is the total number of polarization domains [pie slices in Fig. 7(a)]. Then, in cylindrical coordinates, the screened Coulomb potential is given by

$$\frac{e^{-\kappa|\mathbf{r}-\mathbf{r}'|}}{|\mathbf{r}-\mathbf{r}'|} = \frac{2}{\pi} \sum_{n=0}^{\infty} (2 - \delta_n) \cos[n(\theta - \theta')] \times \int_0^{\infty} dk I_n(x_{<}) K_n(x_{>}) \cos[k(z - z')], \quad (25)$$

where we have the Kronecker delta δ_n ($\delta_n = 1$ if $n = 0$ and $\delta_n = 0$, otherwise). Also, $x_{<,>} = \sqrt{k^2 + \kappa^2} r_{<,>}$ and $r_{<} (r_{>})$ is the smaller (larger) of the polar distances r and r' . Substituting $\rho(\theta)$ from Eq. (24) and Eq. (25) into Eq. (1) yields (after some algebra and an identity for the integral of a single modified Bessel function of the first kind $I_\nu(z)$ [36])

$$F_\rho = \frac{32\pi^2 h^3 P_0^2}{\epsilon\epsilon_0} \sum_{m=0}^{\infty} (-1)^m \int_0^{\infty} du \frac{\sin^2(\frac{u}{2})}{u^2(u^2 + h^2\kappa^2)} \times \int_0^{\frac{R}{h}\sqrt{u^2 + h^2\kappa^2}} dv I_{2m+1+n_\theta}(v) K_{n_\theta}(v), \quad (26)$$

where $K_\nu(x)$ is a modified Bessel function of the second kind. The dominant term in the summation is $m = 0$ and we can make use of the approximations $I_{n_\theta+1}(v) K_{n_\theta}(v) \approx v[4n_\theta(n_\theta + 1)]^{-1} (2v)^{-1}$ for $v \ll n_\theta$ and $v \gg n_\theta$, respectively.

So, what about the elastic and anchoring energy? The total length of domain wall is $2n_\theta R$ so that the total energy of the domain walls is $F_{\text{dw}} = 2n_\theta R f_\pi$, with f_π the linear energy density of the domain walls (e.g., either the solitonic wall or the disclination line pair). Combining the elastic and electrostatic contributions, we find that the total free energy $F = F_\rho + F_{\text{dw}}$ of the ‘‘pie-slice’’ configuration with n_θ cuts (i.e., $2n_\theta$ pie slices) reads

$$\frac{F}{F_0} = \frac{8h\eta_\theta^2}{R} \int_0^{\infty} du \frac{\sin^2(\frac{u}{2}) \Xi_{n_\theta}(\frac{R}{h}\sqrt{u^2 + \kappa^2 h^2})}{u^2(u^2 + \kappa^2 h^2)} + n_\theta, \quad (27)$$

where $F_0 = 2Rf_\pi$ is a characteristic energy, and $\eta_\theta = 2\pi h/\lambda_{\text{dw}}$ is the optimal number of sectors without screening $\eta_\theta = n_\theta^*(\kappa \rightarrow 0)$, and $\Xi_{n_\theta}(z) \equiv \int_0^z I_{n_\theta+1}(z) K_{n_\theta}(z) dz$. The integrations can be evaluated numerically. The plot of the total free energy in Eq. (27) is shown in Fig. 7(b). We see that the total free energy exhibits a minimum at a non-zero value of n_θ , analogously to the plot in Fig. 6(b) for the stripe domains. We thus find that the pie-slice configuration, such as the one shown schematically in Figs. 7(a) and in a micrograph in Fig. 2(a,b), is energetically favorable.

At this point, we can look for the behavior of the inside the integrals in Eq. (26) for large n_θ to get a better sense of the Coulomb energy contribution. This is possible via asymptotic expansions [37]. There are two cases

to consider: $\kappa R \ll n_\theta$ (weak screening) and $\kappa R \gg n_\theta$ (strong screening). We find that, for thin cells compared to the domain size, $h \ll R$,

$$F_\rho \approx \frac{\pi^2 h P_0^2}{\epsilon\epsilon_0} \begin{cases} \frac{hR}{2n_\theta} & \kappa R \ll n_\theta \\ \frac{4\pi}{\kappa^2} \ln\left(\frac{\kappa R}{n_\theta}\right) & \kappa R \gg n_\theta \end{cases} \quad (28)$$

We see that in both cases, this Coulomb energy *decreases* with *increasing* n_θ , in contrast to the elastic and anchoring energies which will increase proportionally to n_θ due to the domain wall formation. One may compare the energetic contribution on the first line of Eq. (28) to Eq. (8), where the dominant contribution to the electrostatic energy scales as $F_\rho \propto I_1(\alpha_0) K_1(\alpha_0) \propto 1/k_z$ for sufficiently small κ . We see here that we get a similar behavior, in that $F_\rho \propto 1/n_\theta$ in Eq. (28). In other words, in both cases, the electrostatic interaction generates an energetic contribution inversely proportional to the ‘‘wave number’’ of the spatial modulation.

We can minimize the total free energy F to find a pretty simple approximate result:

$$n_\theta^* \approx \begin{cases} \frac{2\pi h}{\lambda_{\text{dw}}} & \kappa R \ll n_\theta^* \\ \frac{4\pi^3 h}{R(\kappa\lambda_{\text{dw}})^2} & \kappa R \gg n_\theta^* \end{cases}, \quad (29)$$

where $\lambda_{\text{dw}} = \sqrt{2f_\pi\epsilon\epsilon_0}/P_0$ is the previously-mentioned characteristic length and the large versus small screening conditions have to be checked self-consistently. The value $2n_\theta^*$ should give the ‘‘optimal’’ number of sectors (i.e., \pm polarization domains).

This description, however, is incomplete as we also need to consider what happens very far from the center of the radial aster where the anchoring looks uniform along the local radial direction. Here, we expect to again find parallel striped domains, just as in the stripe domain case considered in the previous subsection: The sample should break up into stripes along the radial direction with characteristic wavelength λ_x^* . We can use the analysis of the striped pattern and imagine that the circumference $2\pi R$ breaks up into segments with wavelength λ_x^* . This corresponds to an optimal number (in the low screening limit $\kappa\lambda_{\text{dw}} \ll \sqrt{h/R}$) of

$$n_\theta^{\text{stripe}} \approx \frac{2\pi R}{\lambda_x^*} \approx 1.2 \frac{R}{\lambda_{\text{dw}}} \sqrt{\frac{h}{L}}, \quad (30)$$

where L is a large dimension (i.e., the full sample length). It is also worth noting that we have not considered the energetic cost of nucleating the domain walls near the aster center where the domain walls get close to each other. This would generate additional elastic distortion, so we might expect that Eq. (29) generally overestimates the number of sectors.

V. QUANTITATIVE COMPARISONS

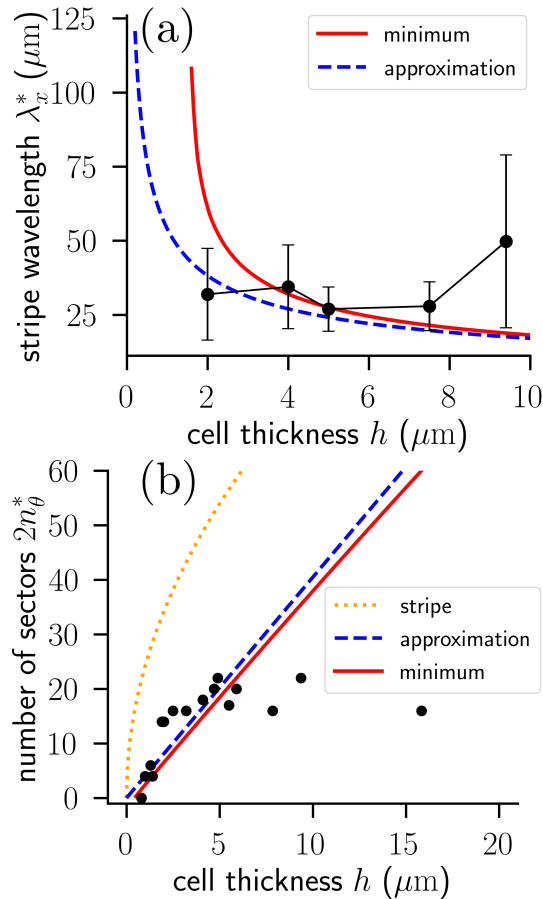


FIG. 8. (a) TD stripe wavelength $\lambda_x^* \approx 2\langle w_{\text{stripe}} \rangle$ for various cell thicknesses h calculated from the average stripe width across a sample with unidirectional, bipolar anchoring. The error bars show the standard deviation over observed stripes. The red solid curve is the wavelength found by minimizing Eq. (20) over $\kappa\lambda_x$ for a fixed $\kappa\lambda_{\text{dw}} = 0.01$ and $\lambda_D = \kappa^{-1} = 10 \mu\text{m}$. The blue dashed line is the approximation in Eq. (21). (b) The number of “pie-slice” sectors (SDs) $2n_\theta^*$ counted out at a distance of $R = 103.6 \mu\text{m}$ from the defect center of a cell pre-patterned with a +1 “aster” defect. The red line corresponds to the sector number evaluated by minimizing the free energy in Eq. (27) with $\lambda_D = \kappa^{-1} = 0.18 \mu\text{m}$ and $\lambda_{\text{dw}} = 0.1 \mu\text{m}$. The blue dashed line is the approximation in Eq. (29) (second line). The orange dotted line is the “stripe” approximation in Eq. (30) with $\lambda_{\text{dw}} = 0.1 \mu\text{m}$, $\lambda_D = 10 \mu\text{m}$ and $L_y = 1 \text{ cm}$.

To compare these theoretical results to experiment, it is necessary to make some estimates for the domain wall energy density f_π which determines the characteristic length λ_{dw} . A key question is how f_π depends on the cell thickness h . For simplicity, we will assume that the walls are the disclination pairs, so that $f_\pi \approx 2K \sim 10 - 1000 \text{ pN}$ is independent of the thickness h . Then, estimating that $P_0 \approx 0.044 \text{ C/m}^2$ for DIO [38] and $\epsilon \approx 10 - 100$, we find the range $\lambda_{\text{dw}} = (2f_\pi\epsilon\epsilon_0)^{1/2}P_0^{-1} \sim 3 \text{ nm} - 30 \text{ nm}$. This is a small length

corresponding to the structure of the domain wall.

We also need to estimate the screening length $\lambda_D = \kappa^{-1}$. This is not necessarily constant throughout the sample as different amounts of free charge may accumulate throughout the sample, so the bound charges may not be uniformly cancelled. For example, in the stripe case (UDs and TDs), the screening effects would be most important near the domain or cell boundary. On the other hand, for the radial slices (SDs), the screening near the +1 defect would be more relevant. Moreover, as discussed previously, the screening depends on the sample preparation protocol, such as the cooling rate. Thus, we might expect different values of κ depending on the sample considered.

For the stripe patterns (TDs), we measure the stripe widths w_{stripe} across a cell over a distance of about $500 \mu\text{m}$ [see Fig. 1(a-d)]. The average $\langle w_{\text{stripe}} \rangle$ and standard deviation $\sqrt{\langle w_{\text{stripe}}^2 \rangle - \langle w_{\text{stripe}} \rangle^2}$ for various cell thicknesses between $2 \mu\text{m}$ and $10 \mu\text{m}$ are shown as the data points and error bars, respectively, in Fig. 8(a). To compare to theory, we minimize Eq. (20) with respect to $\kappa\lambda_x$ while varying the parameters κ and λ_{dw} . The red dashed line in Fig. 8(a) corresponds to $\kappa\lambda_{\text{dw}} = 0.01$ and $\lambda_D = \kappa^{-1} = 10 \mu\text{m}$, with $L_y = 1 \text{ cm}$ the full sample size. This is a relatively large screening length and a correspondingly large $\lambda_{\text{dw}} \approx 100 \text{ nm}$. This suggests that the domain walls between polarization domains cost more energy than our simple estimate suggests and that the depolarization fields at the sample boundaries are not strongly screened. The zero screening prediction ($\kappa \rightarrow 0$) is also shown in Fig. 8(a).

For the pie-slice domains in the +1 aster defect cell, we count the number of domains out at a radius $R \approx 100 \mu\text{m}$ away from the center of the defect. We then compare to the theoretical result for $2n_\theta^*$ given by Eq. (29). We find that the $\kappa R \ll n_\theta^*$ result cannot describe the data without introducing anomalously large values of either the elastic constant K or the dielectric constant ϵ . Instead, the data is more consistent with large screening $\kappa R \gg n_\theta^*$. Using $\lambda_{\text{dw}} = 100 \text{ nm}$ as for the stripe case, we find that $\lambda_D = \kappa^{-1} = 0.13 \mu\text{m}$ does a reasonable job describing the data, as shown by the red curve [calculated by numerically minimizing the free energy in Eq. (27)] and the blue curve [calculated using the second line in Eq. 29, shown in Fig. 8(b)]. We also checked whether the approximation in Eq. (30) yields reasonable results using the same value $\lambda_D = 10 \mu\text{m}$ (and $L_y = 1 \text{ cm}$) used for the stripes. We see that this approximation overestimates the number of sectors, suggesting that the radial sector pattern formation indeed comes from unscreened bound charge generated by the +1 defect.

In summary, the quantitative comparisons for the pie slice (SD) and stripe domain (TD) patterns yield rather different results for the Debye screening length λ_D . This could be due to the different nature of the patterns: the stripes are generated due to uncompensated bound charges at the sample boundaries while the radial pie slices form due to a non-vanishing bound charge density at the +1 defect center. It is likely that the free ions

are able to screen the charge better at the defect center. It would be interesting to systematically vary the free ion concentration in the samples in order to get a better comparison to the theoretical results, which depend sensitively on λ_D .

VI. CONCLUSIONS

We have demonstrated that the N_F spontaneously forms a spatial modulation due to the competition between Coulomb and elastic interactions. The long-range Coulomb interactions generate a large energetic penalty for regions with uniform \mathbf{P} . This can come from either bound charge in the bulk of the system due to a nonvanishing divergence $\nabla \cdot \mathbf{P}$ or due to uncompensated charges at the edges of domains. Overall, the Coulomb interactions tend to create regions of opposing \mathbf{P} directions.

On the other hand, reorientations of the polarization direction incur elastic energy costs in the form of twists, defect lines, or domain walls. The competition between these two effects creates a variety of domain patterns that depend strongly on the cell thickness and the ionic content. In micron-thin N_F cells with the same uniform direction of apolar anchoring at the top and bottom plates, the patterns are formed by domains with a uniform polarization that flips by π in transition from one domain to the next, see Figs. 1 (a-d), 2(a,b), 4(a), and 7(a). In thicker cells, the neighboring domains, in addition to surface flips, show left- and right-handed π twists of polarization around the axis perpendicular to the cell, see Figs. 1(e-j), 3, and 6(a). The lateral extent of these domains in the experiments and in the model (λ_x^*) is typically larger than the film thickness and ranges from microns to tens of microns. The length depends on system parameters including elastic constants, polarization density, and the Debye screening length κ^{-1} . The model derives analytic expressions for the critical concentration of ions above which the domain patterns do not form and for a critical thickness of the cell below which the domains are not twisted. The surface anchoring pattern is another factor that greatly affects the domain structure.

In particular, we considered thin cells pre-patterned with a +1 radial “aster” defect. Here, the system breaks up into “pie-slice” domains due to the bound charge distribution $\rho = -\nabla \cdot \mathbf{P} \propto 1/r$, decaying with distance r from the defect core. The theoretically predicted number of pie slices ($2n_\theta^*$) is consistent with the experiment and with the idea that the screening effect in the pre-patterned splay is stronger than in the case of uniform surface anchoring.

In the future, we hope to test the theory more stringently by systematically varying the free ion concentration (and κ , consequently), which is predicted to have the strongest effect. It would also be interesting to see what happens in a pre-patterned cell with a variety of regions both with vanishing and non-zero $\rho = -\nabla \cdot \mathbf{P}$. We would expect to see “grain boundaries” between different kinds of domain patterning. Finally, an important unexplored question is the nature of the domain wall between π -twisted domains. The π -twist soliton considered here (and in [7] in more detail) is likely only present for very thin cells which do not have the π -twist along the z -direction. If the domains have counter-rotating twists, as illustrated in Fig. 6(a), then the domains likely consist of other structures, such as pairs of surface disclinations or more discontinuous transitions between polarization orientations [8]. It would be interesting to investigate if it is also possible to have adjacent domains with the same twist chirality along the z direction. In this case, one would expect a discontinuity in \mathbf{P} orientation along the domain wall and possible uncompensated charge. This would then introduce additional dipolar interactions between pairs of domain walls, leading to an even richer behavior.

ACKNOWLEDGMENTS

We thank J. Selinger and L. Paik for helpful discussions. PK and ODL acknowledge the support of NSF grant DMR-2341830.

-
- [1] R. J. Mandle, S. J. Cowling, and J. W. Goodby, *Phys. Chem. Chem. Phys.* **19**, 11429 (2017).
 - [2] H. Nishikawa, K. Shiroshita, H. Higuchi, Y. Okumura, Y. Haseba, S.-i. Yamamoto, K. Sago, and H. Kikuchi, *Adv. Mater.* **29**, 1702354 (2017).
 - [3] N. Sebastián, L. Cmok, R. J. Mandle, M. R. de la Fuente, I. Drevenšek Olenik, M. Čopič, and A. Mertelj, *Phys. Rev. Lett.* **124**, 037801 (2020).
 - [4] X. Chen, E. Korblova, D. Dong, X. Wei, R. Shao, L. Radzihovsky, M. A. Glaser, J. E. MacLennan, D. Bedrov, D. M. Walba, et al., *Proc. Natl. Acad. Sci. U.S.A.* **117**, 14021 (2020).
 - [5] A. Adaka, M. Rajabi, N. Haputhantrige, S. Sprunt, O. D. Lavrentovich, and A. Jáklí, *Phys. Rev. Lett.* **133**, 038101 (2024).
 - [6] A. Erkoreka and J. Martinez-Perdiguero, *Phys. Rev. E* **110**, L022701 (2024).
 - [7] B. Basnet, M. Rajabi, H. Wang, P. Kumari, K. Thapa, S. Paul, M. O. Lavrentovich, and O. D. Lavrentovich, *Nat. Commun.* **13**, 3932 (2022).
 - [8] P. Kumari, B. Basnet, H. Wang, and O. D. Lavrentovich, *Nat. Commun.* **14**, 748 (2023).
 - [9] K. G. Hedlund, V. Martinez, X. Chen, C. S. Park, J. E. MacLennan, M. A. Glaser, and N. A. Clark, *Phys. Chem. Chem. Phys.* **27**, 119 (2025).
 - [10] P. Kumari, B. Basnet, M. O. Lavrentovich, and O. D. Lavrentovich, *Science* **383**, 1364 (2024).
 - [11] A. Khachatryan, *J. Phys. Chem. Solids* **36**, 1055 (1975).
 - [12] Y. Guo, M. Jiang, C. Peng, K. Sun, O. Yaroshchuk,

- O. Lavrentovich, and Q.-H. Wei, *Adv. Mater.* **28**, 2353 (2016).
- [13] Y. Guo, M. Jiang, C. Peng, K. Sun, O. Yaroshchuk, O. D. Lavrentovich, and Q.-H. Wei, *Crystals* **7**, 8 (2016).
- [14] N. Sebastián, M. Čopič, and A. Mertelj, *Phys. Rev. E* **106**, 021001 (2022).
- [15] L. Paik and J. V. Selinger, arXiv preprint arXiv:2408.10347 (2024).
- [16] F. Vafa and A. Doostmohammadi, arXiv preprint arXiv:2501.04769 (2025).
- [17] R. J. Mandle, S. J. Cowling, and J. W. Goodby, *Chem. Eur. J.* **23**, 14554 (2017).
- [18] X. Chen, V. Martínez, E. Korblova, G. Freychet, M. Zhernenkov, M. A. Glaser, C. Wang, C. Zhu, L. Radzihovsky, J. E. MacLennan, et al., *Proc. Natl. Acad. Sci. U.S.A.* **120**, e2217150120 (2023).
- [19] B. Zhong, M. Shuai, X. Chen, V. Martínez, E. Korblova, M. A. Glaser, J. E. MacLennan, D. M. Walba, and N. A. Clark, *Soft Matter* (2025), advance Article.
- [20] P. M. Rupnik, E. Hanžel, M. Lovšin, N. Osterman, C. J. Gibb, R. J. Mandle, N. Sebastián, and A. Mertelj, *Sci. Adv.* **2025**, 2414818 (2025).
- [21] Z. Ma, M. Jiang, A. Sun, S. Yi, J. Yang, M. Huang, S. Aya, and Q.-H. Wei, arXiv preprint arXiv:2411.12336 (2024).
- [22] N. A. Clark, X. Chen, J. E. MacLennan, and M. A. Glaser, *Phys. Rev. Res.* **6**, 013195 (2024).
- [23] P. G. de Gennes and J. Prost, *The Physics of Liquid Crystals* (Oxford Univ. Press, New York, 1995), 2nd ed.
- [24] I. A. Lukyanchuk, A. G. Razumnaya, S. Kondovych, Y. A. Tikhonov, and V. M. Vinokur, arXiv preprint arXiv:2406.19728 (2024).
- [25] I. A. Lukyanchuk, A. G. Razumnaya, S. Kondovych, Y. A. Tikhonov, B. Khesin, and V. M. Vinokur, *Phys. Rep.* **1110**, 1 (2025).
- [26] A. Fernandez, M. Acharya, H.-G. Lee, J. Schimpf, Y. Jiang, D. Lou, Z. Tian, and L. W. Martin, *Adv. Mater.* **34**, 2108841 (2022).
- [27] S. K. Streiffer, J. A. Eastman, D. D. Fong, C. Thompson, A. Munkholm, M. V. R. Murty, O. Auciello, G. R. Bai, and G. B. Stephenson, *Phys. Rev. Lett.* **89**, 067601 (2002).
- [28] L. Feigl, P. Yudin, I. Stolichnov, T. Sluka, K. Shapovalov, M. Mtebwa, C. S. Sandu, X.-K. Wei, A. K. Tagantsev, and N. Setter, *Nat. Commun.* **5**, 4677 (2014).
- [29] C. Kittel, *Phys. Rev.* **70**, 965 (1946).
- [30] G. B. Stephenson and K. R. Elder, *J. Appl. Phys.* **100**, 051601 (2006).
- [31] L. Landau and E. Lifshits, *Phys. Zeitsch. der Sow.* **8**, 153 (1935).
- [32] C. Kittel, *Phys. Mod. Phys.* **21**, 541 (1949).
- [33] S. Yi, Z. Hong, Z. Ma, C. Zhou, M. Jiang, X. Huang, M. Huang, S. Aya, R. Zhang, and Q.-H. Wei, *Proc. Natl. Acad. Sci. U.S.A.* **121**, e2413879121 (2024).
- [34] P. Kumari, O. Kurochkin, V. G. Nazarenko, O. D. Lavrentovich, D. Golovaty, and P. Sternberg, *Phys. Rev. Res.* **6**, 043207 (2024).
- [35] Z. Zhuang, J. E. MacLennan, and N. A. Clark, *Proc. Soc. Photo Opt. Instrum. Eng.* **1080**, 110 (1989).
- [36] I. S. Gradshteyn and I. M. Ryzhik, *Table of Integrals, Series, and Products* (Academic Press, Cambridge, 2007), 7th ed.
- [37] A. Sidi and P. E. Hoggan, *Int. J. Pure Appl. Math.* **71**, 481 (2011).
- [38] H. Nishikawa, K. Shiroshita, H. Higuchi, Y. Okumura, Y. Haseba, S. Yamamoto, K. Sago, and H. Kikuchi, *Adv. Mater.* **29**, 1702354 (2017).